RSC Advances

PAPER

View Article Online
View Journal | View Issue

Cite this: *RSC Adv.*, 2017, **7**, 18658

Self-assembled nanoporous graphene quantum dot-Mn_3O_4 nanocomposites for surface-enhanced Raman scattering based identification of cancer cells†

Chuanqing Lan, Jingjin Zhao, Liangliang Zhang,* Changchun Wen, Yong Huang and Shulin Zhao*

Received 23rd January 2017
Accepted 20th March 2017

DOI: 10.1039/c7ra00997f

rsc.li/rsc-advances

Surface-enhanced Raman scattering (SERS) as an unequivocal surface-sensitive technique has been considered one of the most powerful tools for identifying molecular species. However, the SERS active substrates have mainly been confined to some research on noble metals such as Pd, Au, Ag and Cu. In the present study, we describe the self-assembly of graphene quantum dots (GQDs) with Mn_3O_4, and the use of the resulting nanocomposite in the signal enhancement of Raman spectroscopy for non-noble metal SERS active substrates. GQDs can be used to enhance the Raman signal *via* an electromagnetic mechanism, but their intrinsic fluorescence overlaps with the Raman signal. Previous studies regarding tuning the energy level and energy gap to change the optical properties of GQDs mainly focused on doping heteroatoms. Assembling Mn_3O_4 with GQDs in nanocomposites can change the energy level of the material, and quench the fluorescence of the GQDs and adsorbed molecules to improve the Raman signal and noise. The large enhancement factor of 2.06×10^4, compared to that of graphene and graphene oxide, can be explained using a photon-induced charge transfer resonance model, which means that it not only can be used in small molecule identification but can also be used to discriminate cancer cells and normal cells.

Introduction

Raman spectroscopy is an important tool for molecular identification; its characteristics are rapid, precise and robust. Because the chemical structure often corresponds to the vibrational information of the molecules, a molecular finger-print can be identified by Raman spectroscopy.[1] Therefore, it is a very efficient and non-destructive method for investigating art and monitoring chemical reactions.[2,3] However, it is limited by the small molecular resonance cross-sections of most molecules that lead to weak Raman signals.[4] The surface-enhanced Raman scattering (SERS) technique can enhance the signal by adhering molecules onto metal surfaces, nanostructures or other materials as a substrate,[5] which can greatly enhance Raman signals relative to normal Raman spectroscopy.[6] Developing substrates to enhance Raman signals has been an important research focus during the last few decades.[7] The SERS mechanism is comprised of both an electromagnetic mechanism (EM) and a chemical mechanism (CM). The CM involves charge transfer between the molecule and the substrate and possesses an enhancement factor (EF) of 10–100. The EM mainly relies on the surface plasmon and possesses an enhancement factor of 10^4–10^7.[6] The high EF of SERS mainly occurs with coinage metal substrates, such as Pd,[8] Au, Ag and Cu,[6,9] because the plasmon resonance frequencies of these materials lie within the excitation wavelengths used in Raman spectroscopy. However, these metal substrates often have undesirable features such as high cost, poor stability[10] and low biocompatibility.[11] It is therefore an important goal to identify and characterize alternative SERS substrates that overcome these drawbacks.[12,13]

Graphene-enhanced Raman scattering (GERS)[14] occurs solely through chemical enhancement without an additional electromagnetic enhancement.[15] GERS provides a cleaner SERS baseline (lower noise) through surface passivation that in turn protects the detected molecule from photocarbonization and photobleaching under the laser beam compared with noble metal substrates. Therefore, the GERS-related enhancement is greater than that offered by a bare noble-metal substrate.[16] However, the EFs are relatively small. For a graphene substrate, for example, only a 2- to 17-fold EF was observed.[14] Graphene substrates coated with noble-metal nanoislands (Ag and Au) also provided only moderate Raman enhancement: 7.55×10^2

State Key Laboratory for the Chemistry and Molecular Engineering of Medicinal Resources, Key Laboratory of Ecology of Rare and Endangered Species and Environmental Protection of Ministry Education, Guangxi Normal University, Guilin, 541004, China. E-mail: zhaoshulin001@163.com; liangzhang319@163.com

† Electronic supplementary information (ESI) available: Experimental calculations, supplementary figures and tables. See DOI: 10.1039/c7ra00997f

for GERS-Ag and 85 for GERS-Au.[16] Various works have investigated the relationship between the chemical structure of graphene and the SERS performance using graphene oxide (GO),[12] graphene-quantum dot (GQDs) assembled nanotubes[17] and meshed graphene.[18] These studies tell us that the edge effects of graphene in the enhancement of the Raman signal may be an important focus of GERS research.

GQDs possess unique optoelectronic properties that differ from bulk graphene sheets as a result of quantum confinement[19] and edge effects[20] that are present in graphene structures smaller than 100 nm.[21] Furthermore, theoretical calculations suggest that GQDs have surface plasmon frequencies similar to those of metal nanoparticles, in contrast to graphene sheets, which do not have these frequencies.[22] In other words, GQDs can be applied to SERS using an EM. However, GQDs that possess the properties that give rise to quantum confinement effects are also prone to fluorescence. For such systems, the excitation wavelength-dependent fluorescence properties[23] and upconversion[24] would significantly disturb the Raman signal because the fluorescence signal would cover the Raman peaks in Raman spectroscopy. Thus, reducing the fluorescence background of the Raman spectrum can improve the detection sensitivity and make the Raman peaks more visible.[25] By Lombardi's model,[26] charge transfer is important because SERS would not occur with surface plasmon resonance without charge transfer, and it is therefore important to investigate the effect of introducing charge transfer from a suitable additive to the GQDs.

Photo-induced charge transfer is charge transfer induced by light. Because of the importance of this process in understanding the photophysics and photochemistry of excited states in organic molecules, it is studied extensively in many scientific fields. The product of charge transfer can be metastable because of the fast delocalization of the charges produced on the donor and acceptor (not limited to molecules).[27] Based on the photo-induced charge transfer mechanism, a series of chemical and biological sensors,[28] photovoltaic devices,[29] photocatalysts,[30] photodynamic and photothermal therapy nanomaterials,[31] and Raman enhancement substrates have been developed.[32] Among the SERS processes, photo-induced charge transfer is an important mechanism that occurs between the molecule and the substrate and can enhance the Raman signal. It is the key factor in making GQDs an appropriate Raman substrate. Photo-induced charge transfer applied for Raman enhancement requires a charge transfer energy between dye molecules and substrate that matches the incident light energy.[33] However, the Fermi level (in a vacuum) of GQDs is about −4.2 eV to −4.4 eV,[34] and the energy gap is approximately 0.4 eV.[22] This also limits application of GQDs to Raman technology. Methods for tuning the energy level and gap have mainly focused on doping with heteroatoms.[35,36] However, the effects are confined and cannot satisfy the demand of charge transfer energy that matches the incident light energy.

Self-assembly is an efficient strategy for making ensembles of nanostructures. The design of components that organize themselves into desired patterns and functions is key to the successful application and control of the self-assembly process.[37] An assembled nanoscale composite can possess structure-controlled optical and electronic properties, and the potential for morphological diversity extends the functions of the material in electronic, electrochemical, optical and sensing applications.[38–40] Reports of nanocomposites that use graphene as a building block include materials self-assembled using DNA for self-healing,[41] using TiO_2 for photocatalysis,[42] using transition-metal oxides for electrochemical functionality,[43,44] using noble metals as organic catalysts,[45] and using ferrite nanoparticles for separation and purification.[46] To the best of our knowledge, graphene metal oxide nanocomposites for use in SERS have not been reported. Metal or metal oxide nanoparticles were deposited on the surface of graphene, and a 3D net structure of a graphene nanocomposite was formed by self-assembly. In this case, the relationship between nano-particles and graphene is not clear. Because graphene is a material with a 2D planar structure (approximately micron scale), which is significantly larger than the nanoparticles, GQDs are more readily observed with respect to the nanoparticles. Transmission electron microscopy (TEM) images illustrate that the nanoparticles are present on the graphene surface,[42,46] but it is not clear how the 3D network structure is connected. Understanding how the 3D graphene networks are connected is important so that new self-assembled graphene materials may be designed in the future.

One potentially suitable additive for the purpose of facilitating charge transfer in a SERS system is Mn_3O_4, which has an extensive oxide system with oxidation states ranging from +2 to +4 valences. Mn_3O_4 is widely used in electrodes for electrolytic supercapacitors,[47] and the charge transfer process is correlated with electrode materials that can be used in Raman spectroscopy.[48] Mn_3O_4 can exhibit absorption in the UV and visible regions from 220–730 nm owing to the combination of $O^{2-} \rightarrow$ Mn ion charge transfer and the crystal field d → d transition,[49] and as such, it has attracted the interest of researchers.[50,51]

Herein, we describe for the first time a one-pot synthesis of a GQD–Mn_3O_4 nanocomposite using multi-walled carbon nanotubes (MWCNTs) as a starting material. MWCNTs were cut into pieces (GQDs) by $KMnO_4$. Then, the GQDs were combined with manganese ions to form the GQD–Mn_3O_4 nanocomposite through a process of 0D to 3D self-assembly. The purpose of using Mn_3O_4 was not only to connect the GQDs but also to quench the fluorescence of the GQDs as Mn_3O_4 can efficiently suppress the Raman spectrum fluorescence back-ground. Using Rhodamine B (RhB) as a Raman-active molecule, an EF as high as 2.06×10^4 was obtained. Compared to the EFs of previously reported GERS substrates and many semiconductor substrates, this is an approximately 2 orders of magnitude improvement in the performance of graphene SERS substrates. The prepared GQD–Mn_3O_4 nanocomposite possesses very good biocompatibility, which can be applied for SERS to discriminate cancer cells and normal cells (HeLa, HepG-2 cell line and 7702 cell line) for potential diagnostic applications.

Experimental

Chemicals and materials

MWCNTs (10–20 nm in diameter with lengths < 2 μm) were obtained from Shenzhen Nanotech Port Co., Ltd. (Shenzhen,

China). HPLC grade acetonitrile (J&K China). Tetrabutylammonium perchlorate, $KMnO_4$, H_2SO_4, NaOH and RhB were of analytical grade and were used as received without further purification. Water were prepared with deionized water (>18.2 MΩ cm) from a Direct-Q system (Millipore U.S.A.).

Preparation of GQD–Mn_3O_4 nanocomposites

The synthesis route for the GQD–Mn_3O_4 nanocomposite was shown in Fig. 1A. MWCNTs (50 mg) were suspended in 50 mL of concentrated H_2SO_4 with sonication for 12 h. $KMnO_4$ (500 mg) was then added, and the mixture was stirred for 1 h at room temperature. The mixture solution was then heated to 55 °C for 30 min, after which the temperature was increased to 65 °C for 1 h. Afterwards the temperature was increased to, and then stabilized at, 70 °C for 1 h. It was subsequently allowed to cool to room temperature, and poured onto 100 mL of ice and add 2 mL of 30% H_2O_2. After centrifugation, the supernatant was adjusted to a pH of 6–7 to induce precipitation, followed by centrifugation again, washing several times and drying.

Cell culture

The 7702, HepG-2 and HeLa cells (purchased from China Center for Type Culture Collection) were grown in a humidified atmosphere containing 5% CO_2 at 37 °C in RPMI 1640 medium (Gibco Company, USA) supplemented with 10% fetal bovine serum (CellMax, China), 100 mg mL^{-1} streptomycin and 100 units per mL penicillin (Solarbio, China).

Characterization

UV-Vis spectra were recorded on a Cary 60 UV-Vis-NIR spectrophotometer (Agilent, U.S.A.). Raman spectra were acquired on a Renishaw 2000 model confocal microscopy Raman spectrometer (Renishaw, United Kingdom) with 514.5 nm wavelength incident-laser light and a power of approximately 5 mW. X-ray photoelectron spectroscopy (XPS) measurements were performed using an ESCALAB-MKII spectrometer (VG Co., United Kingdom) with Al Kα X-ray radiation as the X-ray source for excitation. The sample for XPS characterization was deposited onto a Si wafer. X-ray diffraction (XRD) spectra were obtained on a D8 Advance (Germany) using Cu Kα (1.5406 Å) radiation.

Transmission electron microscopy (TEM) and high-resolution transmission electron microscopy (HRTEM) images were obtained using a TECNAI G2 high-resolution transmission-electron microscope (Holland) with an accelerating voltage of 200 kV. The sample for TEM characterization was prepared by placing a drop of prepared solution on a carbon-coated copper grid and drying at room temperature. Scanning electronic microscopy (SEM) images were obtained using a Quanta FEG 250. The sample was dropped onto a Si wafer, allowed to evaporate and then a conductive Au coating was applied.

The fluorescence experiment was carried out using a Perkin Elmer (U.S.A.) LS-55 Molecular Spectroscopy system. FTIR spectra were recorded using a Perkin Elmer (U.S.A.) Spectrum Two™ IR spectrometer. Fluorescence lifetime data were obtained using HORIBA JobinYvon FluoroLog-3 TCSPC (France). Electrochemical data were recorded using a CHI660C workstation (Shanghai, China).

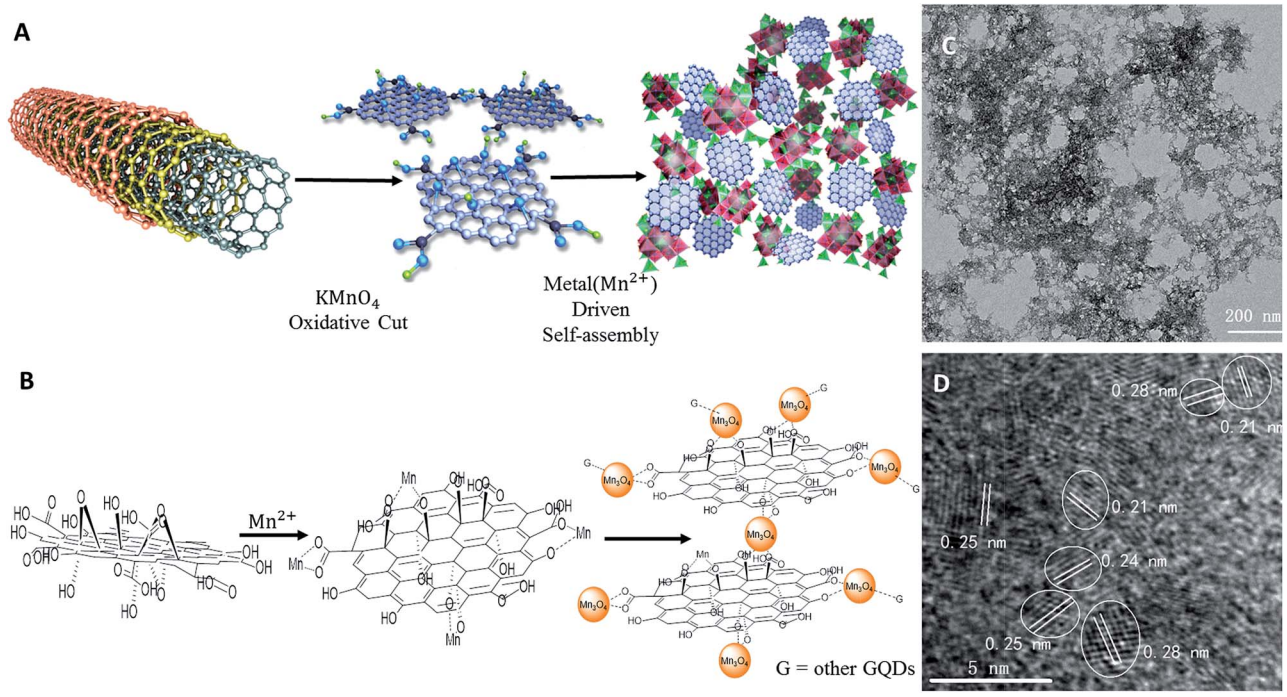

Fig. 1 (A) The synthesis route for the GQD–Mn_3O_4 nanocomposite using MWCNTs as the precursor of GQDs. (B) The formation mechanism for the GQD–Mn_3O_4 nanocomposite. (C) TEM image of the GQD–Mn_3O_4 nanocomposite. (D) HRTEM image of the GQD–Mn_3O_4 nanocomposite.

Electrochemical properties were measured using cyclic voltammetry with glassy carbon as the working electrode, platinum wire as the counter electrode and a double junction saturated calomel electrode as the reference electrode. The triple electrode system was in dry, HPLC grade, argon-purged acetonitrile and 0.1 m tetrabutylammonium per chlorate electrolyte solution. The sample was dropped onto the working electrode and dried under vacuum at 60 °C for 1 h. The initial scan voltage was 1.8 V, high voltage was 1.8 V, low voltage was −2.0 V and the scan rate was 0.05 V s^{-1}. The data were recorded on a CHI660C workstation.

Results and discussion

Characterization of GQD–Mn_3O_4 nanocomposite

We prepared the GQD–Mn_3O_4 nanocomposite using a one-pot synthesis approach. The synthesis process is shown in Fig. 1A. MWCNTs were oxidatively cut by $KMnO_4$ in the presence of H_2SO_4 (ref. 23) into graphene nano-ribbons (GNRs).[52] The GNRs were then further oxidatively cut into GQDs by $KMnO_4$.[53] At the same time, the $KMnO_4$ was reduced to Mn^{2+}. After the pH value was adjusted to a neutral pH, the GQDs self-assembled with the Mn^{2+} through a GO metal ion-induced self-assembly process.[46]

In strongly acidic conditions, manganese oxide will dissociate into constituent ions, and these building blocks will be dispersed into solution, allowing the nanocomposite to be formed by a metal ion-driven self-assembly process with the GQDs. The GQD–Mn_3O_4 composite was treated with 3 M HCl to destroy the Mn_3O_4 and was characterized by TEM (Fig. S1†). The results confirmed that the GQDs were one of the building blocks of the nanocomposite. The TEM image also demonstrates that the GQDs were well dispersed in the aqueous solution.

By measuring 158 particles, the diameter of the GQDs was determined to be in the range of 2 to 12 nm (Fig. S2†); approximately 71% of the particles were 2–4 nm in diameter. HRTEM (Fig. S3†) showed that the lattice spacing values of the GQDs were 0.21 nm and 0.24 nm, corresponding to the (100) and (112) planes of graphite, respectively.[54,55] To elucidate the structure of the GQD–Mn_3O_4 nanocomposite, TEM characterization was performed (Fig. 1C). As shown in the figure, the GQD–Mn_3O_4 nanocomposite possesses a porous structure. This porous nature is reminiscent of those found in previously reported self-assembled graphene-based materials. However, the scale is different: instead of having pores on the micrometer scale, as seen in other studies (GO–metal oxides composites),[46] the pores of the GQD–Mn_3O_4 nanocomposite are on the submicrometer scale (see SEM images in Fig. 2A). The SEM and TEM images all show that the nanocomposite self-assembled into a porous structure, with sub-200 nm pore sizes. This indicates that changing the scale of the building blocks, such as replacing graphene sheets with GQDs can result in significant morphological changes and potentially tunable pore sizes.

The GQD–Mn_3O_4 nanocomposite was also characterized using HRTEM (Fig. 1D). Each distinct crystal lattice spacing was corresponds to a particular compound and can therefore be used to determine the chemical constituents of the nanocomposite. The crystal lattice spacing values of 0.21 nm and 0.24 nm belong to the GQDs, and the 0.25 nm and 0.28 nm values belong to Mn_3O_4, corresponding to the (211) and (103) plane of Mn_3O_4, respectively.[56,57] After identifying the GQDs and Mn_3O_4, it was determined that the GQD particles connect with the Mn_3O_4 particles. This result is supported by the lattice fringes shown in Fig. 2B. The spacings of the lattice fringes in adjacent particles are 0.21 nm, 0.24 nm and 0.25 nm, and 0.28 nm, which appear to be fused together corresponding to the *d*-spacings of GQDs and Mn_3O_4, respectively. In addition, the self-assembly seems to be randomly oriented. Therefore, in our graphene–metal ion-driven assembly process, the function of the metal oxide nanoparticles is to connect the graphene particles to each other. According to previous research,[58,59] GQDs are similar to GO with epoxy, hydroxyl, carbonyl and carboxyl groups. These functional groups of GQDs attached to the Mn ions, and *in situ* formation of Mn_3O_4 then occurred, as is described in Fig. 1B.

The X-ray diffraction (XRD) pattern (Fig. 2B) shows broad peaks centered at approximately 29°, 32°, 36°, 38°, 44° and 59°, which can be indexed to the (112), (103), (211), (004), (220) and (224) planes, respectively.[60] These data match the crystal lattice spacing values of Mn_3O_4 in the HRTEM image (Fig. 1C). All these reflections were indexed to Mn_3O_4 (ICDD-JCPDS no. 24-0734). The peaks (29° and 32°) of the nanocomposite were located at the same positions as reported for Mn_3O_4 (ref. 49) and graphene–Mn_3O_4 composites.[47,60]

We first identified the peaks of C 1s, O 1s and Mn 2p at 284, 528 and 645 eV, respectively, by X-ray photoelectron spectroscopy (XPS) (Fig. 2C). The high-resolution XPS spectrum of C 1s (Fig. 2D) was used for chemical state analysis, and the signal was deconvoluted to peaks at 284.6 eV, 285.0 eV, 286.3 eV and 288.1 eV, which correspond to C–C/C=C bonds, C–O bonds, C=O bonds and O–C=O bonds. The splitting between the peak of Mn $2p_{3/2}$ and the peak of Mn $2p_{1/2}$ is approximately 11.7 eV (Fig. 2E), which matches reports for Mn_3O_4.[47,60]

When comparing the Fourier transform infrared (FTIR) spectroscopy spectra (Fig. S4†) of the GQDs and the GQD–Mn_3O_4 nanocomposite, many of the same absorption bands appear: the O–H stretching vibration at 3400 cm^{-1}, the C–H stretching vibration at 2924 cm^{-1}, the C=O stretching vibration at 1626 cm^{-1}, the C–H deformation vibration of CH and CH_2 at 1466 cm^{-1}, the C–H deformation vibration of CH_3 at 1386 cm^{-1} and the C–O stretching vibration at 1105 cm^{-1}. However, differences arise in peaks belonging to the octahedral vibration of Mn_3O_4 in the range of 400 cm^{-1} to 700 cm^{-1}. The FTIR spectra agree with those obtained for Mn_3O_4 in previous studies.[49,61–63] The Raman spectrum (Fig. S5†) of the GQDs exhibited two peaks at 1363 cm^{-1} and 1596 cm^{-1}, which are characteristic peaks of graphene. The same two peaks were observed for the GQD–Mn_3O_4 nanocomposite, and the sharp peak seen only in the GQD–Mn_3O_4 nanocomposite sample at approximately 650 cm^{-1} corresponds to the Mn–O vibrations in Mn_3O_4.[58,60]

UV-Vis analysis was performed on the GQDs and the GQD–Mn_3O_4 nanocomposite samples, and the results (Fig. S6†) support the conclusions of the FTIR analysis. The GQDs show support the conclusions of the FTIR analysis. The GQDs show

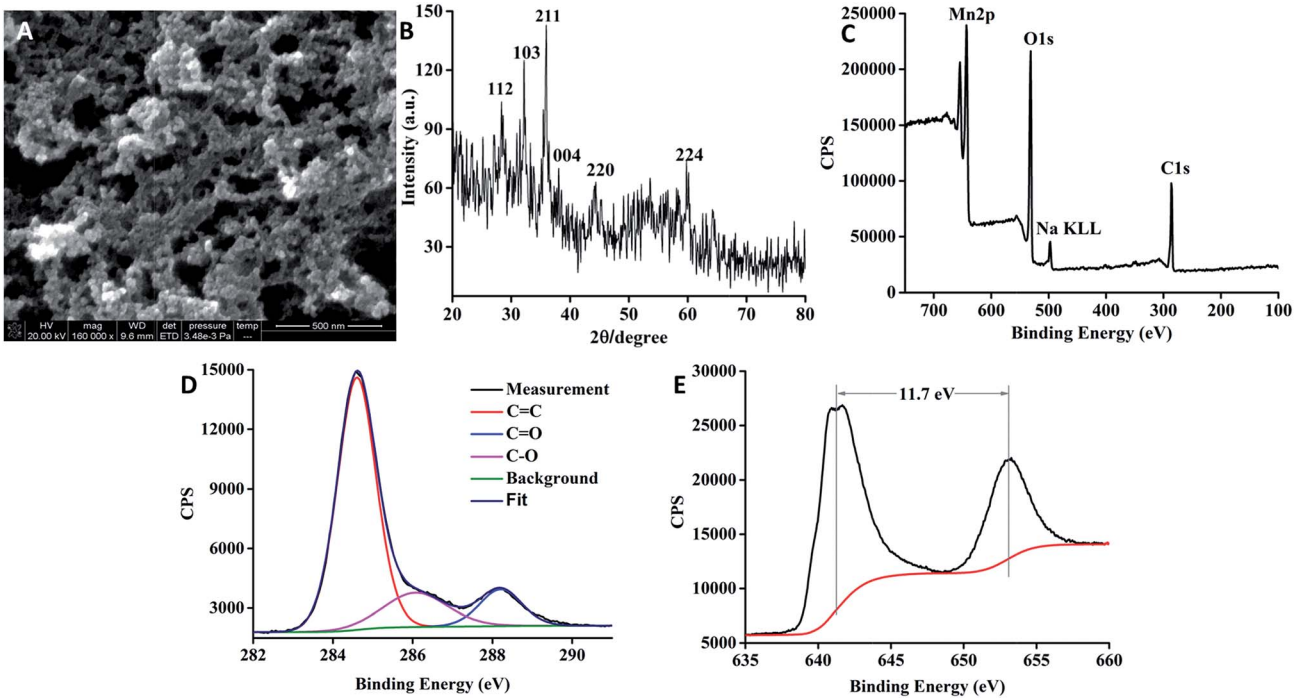

Fig. 2 (A) SEM image of the GQD–Mn_3O_4 nanocomposite. (B) XRD pattern of the GQD–Mn_3O_4 nanocomposite. (C) XPS of the GQD–Mn_3O_4 nanocomposite. (D) XPS of the C 1s. (E) XPS of the Mn 2p.

a peak at 320 nm, which is attributed to the $\pi \rightarrow \pi^*$ absorption.[23] Similar to reports by previous researchers,[49] the GQD–Mn_3O_4 composite, with compositions of MnO–Mn_2O_3 (Mn^{2+} and Mn^{3+}) and 2Mn–MnO_2 (Mn^{2+} and Mn^{4+}), exhibits absorption features from 210 to 730 nm. The three charge transfer transitions $O^{2-} \rightarrow Mn^{2+}$ (210–250 nm), $O^{2-} \rightarrow Mn^{3+}$ (350–390 nm) and $O^{2-} \rightarrow Mn^{4+}$ (440–460 nm) can reasonably be attributed to the d–d crystal field transitions in octahedral Mn with oxidation states ranging from +2 to +4 valance species. Thus, we conclude that Mn^{2+}, Mn^{3+} and Mn^{4+} composed the GQD–Mn_3O_4 nanocomposite. The intense and broad UV-Vis absorption of the nanocomposite is the primary reason that it can quench the fluorescence of the GQDs, as well as that of the dye molecules. Because of the self-assembled nature of the GQDs and Mn_3O_4 species, charge transfer occurs between the GQDs and Mn_3O_4 nanoparticles.

GQD–Mn_3O_4 nanocomposite for Raman enhancement

To explore the Raman enhancement effect, we measured the Raman spectra of RhB on different substrates (glass, GQDs and GQDs–Mn_3O_4 nanocomposite). The substrate in aqueous solution was dropped onto a glass plate. RhB molecules were adsorbed onto the nanocomposite or the GQD substrate simply by depositing the target molecules on the glass film supported samples. Fig. 3 shows the Raman spectra of RhB on the GQD–Mn_3O_4 nanocomposite substrate and those on the GQD and glass substrates for comparison under the same experimental conditions (see methods). Comparison of the three Raman spectra indicates that the glass substrate and the GQD substrate cannot quench fluorescence efficiently, resulting in poor optical contrast. The Raman signal on the glass substrate cannot be observed because of the high fluorescence background. However, on the GQD substrate, Raman peaks can be observed superimposed on the fluorescence background. This indicates SERS activity with the adsorption of RhB molecules on the GQDs. Comparing the fluorescence background intensities of the GQD substrate and the glass substrate, we calculate that the GQDs suppress the fluorescence of RhB by a factor of 3.4 compared to the glass substrate alone. In other words, the GQDs also exhibit Raman enhancement (GERS). A significant degree of fluorescence quenching can be seen for RhB molecules adsorbed onto the GQD–Mn_3O_4 nanocomposite substrate; the fluorescence intensity is lower than that on the GQDs and

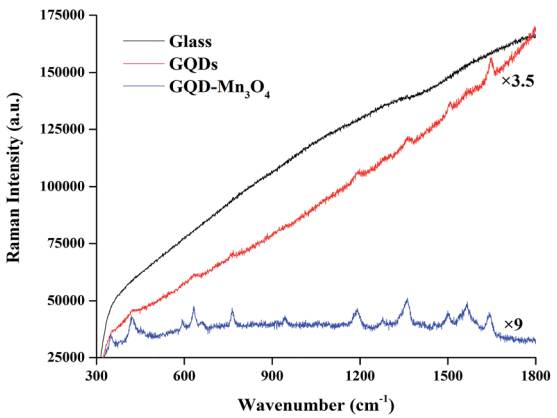

Fig. 3 The Raman signal of RhB (0.6 mM) was recorded on the GQD–Mn_3O_4 nanocomposite film, GQDs and glass.

on glass. Specifically, the intensity of the background fluorescence baseline is decreased approximately 40 times compared to the glass substrate, which improves the Raman/fluorescence ratio and enhances the Raman signal.

Furthermore, even though the baseline is not subtracted from the spectrum, the peaks are clearly visible in the original data. The original spectrum exhibits two peaks at 348 cm^{-1} and 419 cm^{-1}. When carefully checking the original spectrum on the GQD substrate, the two peaks at 351 cm^{-1} and 421 cm^{-1} were determined to be too obscure to be discerned easily because of masking by the fluorescence background. After subtracting the baseline (Fig. S7 and S8†), it was found that the vibrational frequencies of RhB on GQDs and on the GQD–Mn_3O_4 nanocomposite (Table S1,† columns 2 and 4, respectively) were consistent with the SERS results reported previously for graphene and[12] metal substrates[64] and from theoretical calculations.[65,66]

For further investigation, solutions with different concentrations of RhB (concentrations ranging from 1 μM to 600 μM) were dropped onto three different substrates (see Fig. 4A), and the signals were found to improve with increasing concentration. It is interesting that the baseline becomes flatter as the concentration increases. We chose the peaks centered at 419 cm^{-1} as P1, 592 cm^{-1} as P2, 763 cm^{-1} as P3, 943 cm^{-1} as P4, 1190 cm^{-1} as P5, 1361 cm^{-1} as P6 and 1566 cm^{-1} as P7. P1 is assigned to xanthene ring deformation and N–H oscillation, P2 represents –NH wagging, P3 corresponds to C–H out of the plane of the xanthene ring, P4 is xanthene ring and phenyl ring stretching, P5 is assigned to C–H bending of the xanthene ring, P6 is xanthene ring stretching, and P7 is phenyl ring stretching. By fitting these peaks and by applying the Brunauer–Emmett–Teller (BET) model[14] with concentration, this model indicates that the molecules observed a model of multilayer adsorption.[67] It was also found that the relative intensity of some peaks would change with the concentration, according to previous research.[68,69] It can be concluded that the molecular orientation of RhB on the GQD–Mn_3O_4 nanocomposite would change with the concentration of RhB (Fig. 4B). To compare the signal enhancement in a more quantitative manner, we calculated the EF for each case (Fig. S7 and S8†). The largest EF value is 2.06×10^4 at 425 cm^{-1}, and the smallest EF value is 7.95×10^2 at 1649 cm^{-1}. These EFs are among the highest reported for graphene and other non-noble metal SERS substrates (Table S2†).

Photon-induced charge transfer resonance on GQD–Mn_3O_4 Raman enhancement

In the GQD–Mn_3O_4 nanocomposite, the function of Mn_3O_4 is not only to connect the GQDs but also to quench the fluorescence of the GQDs. In other words, the self-assembly of GQDs and Mn_3O_4 change both the morphology and the optical properties of the composite. The 3D fluorescence of GQDs is displayed in Fig. S9† (the Rayleigh scattering peak has been deleted). The maximum excitation is 400 nm, and the emission wavelength is 430 nm. The photoluminescence properties are excitation-wavelength-dependent, as previously reported.[23] The fluorescence emission spectra of the GQDs and GQD–Mn_3O_4 nanocomposite are displayed in Fig. S10.† The GQD–Mn_3O_4 nanocomposite quenched the fluorescence of RhB, and the

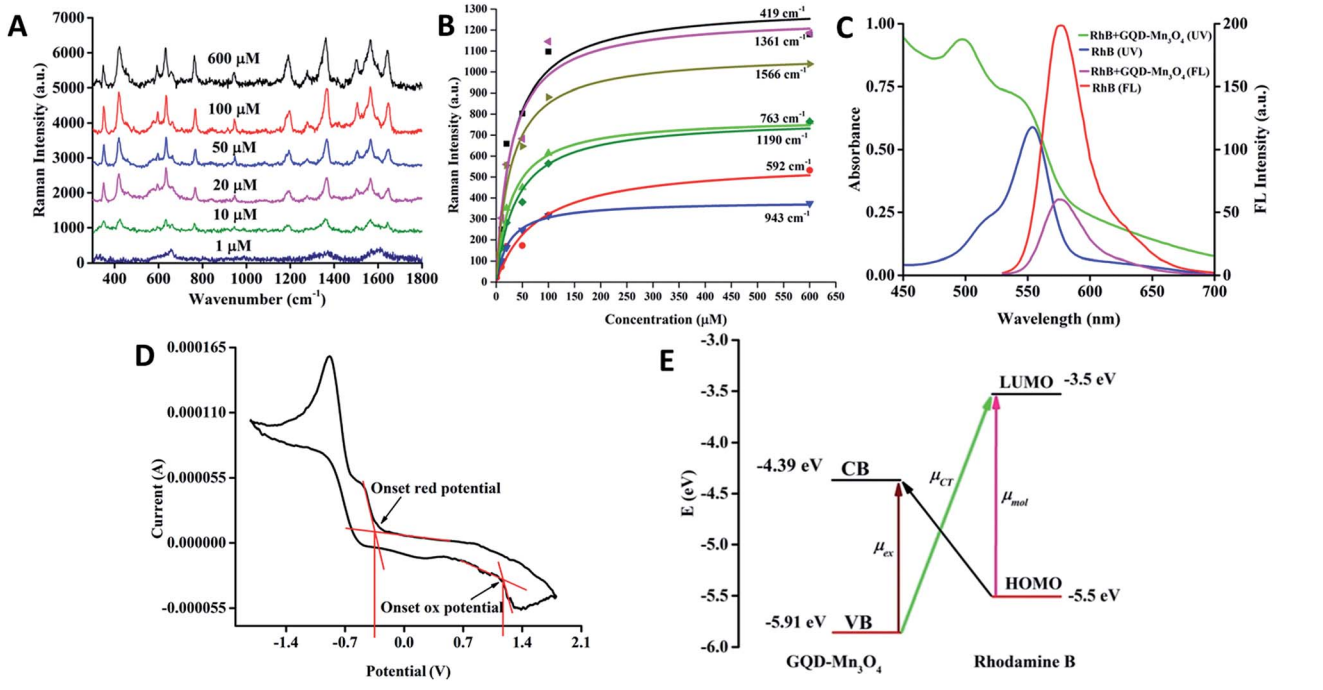

Fig. 4 (A) Raman spectra of RhB (concentration from 1 μM to 600 μM) on the GQD–Mn_3O_4 nanocomposite. (B) The intensity of each vibrational mode and the fitting curve by the BET model for different RhB concentrations (the peak intensities of different concentrations and the fitting curve). (C) The UV-Vis and fluorescence spectra of RhB (1 μM) and RhB (1 μM) + GQD–Mn_3O_4 nanocomposite (0.1 mg mL^{-1}). (D) Cyclic voltammetry diagram of GQD–Mn_3O_4 nanocomposite. (E) Energy level diagram of the GQD–Mn_3O_4–RhB system.

emission of RhB at 580 nm results from excitation at 514 nm in aqueous solution (Fig. 4C). The UV-Vis absorption peaks of RhB in aqueous solution are at 515 nm and 550 nm; with the addition of the nanocomposite (also in aqueous solution), the absorption peaks are blue-shifted to 496 nm and 543 nm. This serves as evidence for the formation of a dye-nanocomposite hybrid with charge transfer occurring between the RhB and the nanocomposite. Additionally, although the emission intensity decreases, the fluorescence lifetime experiment (for which the excitation wavelength is 460 nm) indicates that the lifetime is decreased (1.37 ns to 1.33 ns) when fit by a single-variable exponential decay function (Fig. S11 and S12†). These results suggest that the dye molecules can be thought of as forming a charge transfer complex by interacting with the nanocomposite. Because of the limitations of the experimental conditions, further fluorescence analysis on a faster time scale is needed to investigate the charge transfer process.

GQDs cannot quench the fluorescence of RhB Raman dye when used as a SERS substrate. Moreover, the GQDs' own fluorescence properties, including upconversion and down conversion, decrease the signal-to-noise ratio of the Raman spectrum. By self-assembling with Mn_3O_4, the distance between the GQDs and Mn_3O_4 is small; thus, charge transfer can occur, the fluorescence of the GQDs is quenched, and the nanocomposite can quench the fluorescence of the Raman dye. The lower number of peaks observed for the GQDs than for GQD–Mn_3O_4 can be attributed to the influence of the fluorescence background on the Raman enhancement of the GQDs.

We propose that the Raman-enhancement mechanism of the synthesized nanocomposite is an example of photon-induced charge transfer resonance. As illustrated in Fig. 4E, the energies (vacuum level) of the lowest unoccupied molecular orbital (LUMO) and the highest occupied molecular orbital (HOMO) of RhB are −3.50 eV and −5.50 eV,[70] while the energies (vacuum level) of the valence band (VB) and conduction band (CB) of the GQD–Mn_3O_4 nanocomposite are −5.91 eV edge and −4.39 eV, respectively, as calculated using cyclic voltammetry measurements (Fig. 4D). Compared with a previous study,[71] the VB and CB of GQDs are −5.62 eV and −4.72 eV. By using the photon-induced charge transfer resonance model.[26,33] The charge transfers from the VB to the LUMO at 2.41 eV and from the HOMO to the CB at 1.11 eV are allowed. Charge transfer at 2.4 eV corresponds to 514 nm; thus, the wavelength of the incident laser was selected. The other charge transfer is at 1.1 eV, corresponding to 1127 nm, which is the same as the wavelength of the surface plasmon resonance. With GQDs as the substrate, charge transfer at 2.1 eV corresponds to 590 nm, and the second is at 0.8 eV and corresponds to 1550 nm. According to our knowledge, most Raman spectrometers do not have 590 nm laser beams. Therefore, 514 nm is more convenient than 590 nm.

The Raman enhancement consists of a number of different effects: the molecular resonance (μ_{mol}) of RhB, the excitation resonance (μ_{ex}) of the GQD–Mn_3O_4 nanocomposite and the photon-induced charge transfer resonance (μ_{CT}) from matching the energy levels between the GQDs–Mn_3O_4 nanocomposite and the RhB molecules. In the quantum mechanical model (calculations are given in the ESI†), *via* the vibronic coupling, the ground state $|I\rangle$ with the conduction-band edge $|C\rangle$ and molecular excited state $|K\rangle$ with the valence-band edge $|V\rangle$ of the semiconductor would contribute to the molecular polarizability tensor. When the energy of the incident light equals the charge–transfer transition frequency between the semiconductor valence-band edge and molecular excitation state ($\omega = \omega_{VK}$), the polarizability tensor $\alpha_{\rho\sigma}$ is composed of A, B and C, where the A term, $R_{VK}(\omega)$, represents the plasmon resonance; the B-terms, $R_{ICK}(\omega)$ and $R_{ICV}(\omega)$, represent the charge transfer transitions from the molecule to the semiconductor; and the C-terms, $R_{IVK}(\omega)$ and $R_{KVC}(\omega)$, represent the charge transfer transitions from the semiconductor to the molecule.[33] In this condition ($\omega = \omega_{VK}$), with the incident laser wavelength at 514 nm, the main contributions to the Raman enhancement factors are from the A term $R_{VK}(\omega)$ and the C terms $R_{IVK}(\omega)$ and $R_{KVC}(\omega)$. Therefore, application of the photon-induced charge transfer resonance model to the GQD–Mn_3O_4 nanocomposite experimental results indicates that large EFs could be expected. This is an effective way to design SERS substrates with high enhancement factors, tuning the energy level and energy gap to change the optical properties through self-assembly.

SERS identification of human cancer cells

Biocompatibility is always a major problem with SERS substrates. It limits the biological application because SERS substrates must absorb to the cell surface to obtain a strong signal.[72] Therefore, MTT assays were carried out firstly to evaluate the cytotoxicity of the GQD–Mn_3O_4 nanocomposite to living cells. As expected, the cells viabilities of 7702, HepG-2 and HeLa cell line were estimated to all be greater than 90% upon addition of the GQD–Mn_3O_4 nanocomposite over a wide concentration range of 0–800 μg mL^{-1} (Fig. S13–S15†). To further assess the potential biomedical and diagnostic applications, the GQD–Mn_3O_4 nanocomposite was investigated as a SERS-active substrate for cancer cell identification. The nanocomposite was dropped onto glass-bottomed micro-well dishes, and the cells were then seeded into the dishes. As shown in Fig. 5B–D, the 7702 cell line (normal liver cells), HepG-2 cell line (liver cancer cells) and HeLa cell line (cervical cancer cells) can grow on the substrate. Then, the Raman spectra of the cells were acquired under excitation at 514 nm (Fig. 5A). The Raman spectra showed that the Raman signal of the cells on the glass was very weak, with only the peaks at 470 cm^{-1} and 910 cm^{-1} being observed, and the signals cannot be used to discriminate the 7702 cells with HeLa cells. Although Raman signal of HepG-2 cells was at 470 cm^{-1} and 2900 cm^{-1} which were different from HeLa and 7702 cells, such signal with only two peaks also cannot provide enough information for discriminating these cells. However, under the SERS conditions, the signals of the cells grown on the GQD–Mn_3O_4 nanocomposite were quantifiable compared with the signal on the glass. The SERS peaks of the 7702 cell line were centered at 506 cm^{-1}, 587 cm^{-1}, 929 cm^{-1}, 1084 cm^{-1}, 1394 cm^{-1}, 1584 cm^{-1}, 2401 cm^{-1} and 3087 cm^{-1}. The SERS peaks of the HeLa

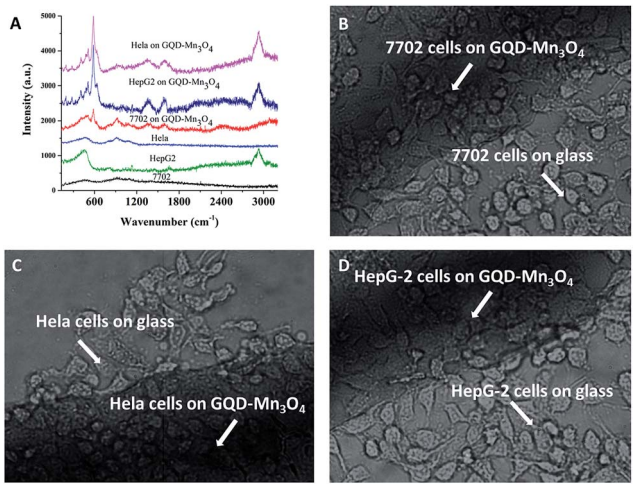

Fig. 5 (A) Raman spectra of the HepG-2, HeLa and 7702 cell line on the GQD–Mn_3O_4 nanocomposite and on the glass. (B) Image of 7702 cells grown on the GQD–Mn_3O_4 nanocomposite. (C) Image of Hela cells grown on the GQD–Mn_3O_4 nanocomposite. (D) Image of HepG-2 cells grown on the GQD–Mn_3O_4.

cell line were centered at 194 cm^{-1}, 278 cm^{-1}, 481 cm^{-1}, 512 cm^{-1}, 585 cm^{-1}, 909 cm^{-1}, 1347 cm^{-1}, 1602 cm^{-1} and 2935 cm^{-1}. The SERS peaks of the HepG-2 cells line were similar to HeLa, and centered at 2401 cm^{-1} which was same as 7702 cell line. Obviously, the Raman peaks between the two types of cells (cancer and normal) are very different. To determine a relationship between cancer and the signal, the Raman spectra of the cells were divided into two parts: the protein and lipid bands and the DNA/RNA bands.[73] The DNA/RNA bands are observed from 1200 cm^{-1} to 1700 cm^{-1} (although the Raman shift of DNA/RNA was centered at 740 cm^{-1}, the Raman signal of the cells on the GQD–Mn_3O_4 did not display the peak at 740 cm^{-1}), and the protein/lipid bands are observed from 2800 cm^{-1} to 3000 cm^{-1} and from 900 cm^{-1} to 1200 cm^{-1}. Generally, the protein levels of tumorigenic cells are higher than those of normal cells.[73] Therefore, the lipid/protein–DNA/RNA ratio can be evaluated to identify the cancer cells. The lipid/protein–DNA/RNA ratio of HeLa and HepG-2 cells is obviously higher than that of 7702 cells. Because the cells were growing on the surface of the substrates, we believe that this can be a useful tool to investigate the surface functional groups of cells using Raman spectra. These groups relate to the biochemical properties of cells and will help to further medical research and drug discovery. As shown in Fig. 5A, the SERS intensity at 585 cm^{-1} was very high in the HeLa cells (the same as HepG-2 cells), and a new peak at 2935 cm^{-1} was observed, indicating that the GQD–Mn_3O_4 nanocomposite can be used as an active substrate for SERS identification of human cancer cells. Compared with other Raman substrates, especially noble metal substrates, GQD–Mn_3O_4 nanocomposites present many more advantages, such as a simple synthesis, a label-free analysis and excellent biocompatibility. This is very important for biomedical applications of SERS.

Conclusions

In summary, we have described a one-pot synthesis of a GQD–Mn_3O_4 nanocomposite *via* self-assembly from MWCNT precursors. The function of Mn_3O_4 is not only to connect the GQDs but also to quench the fluorescence of the GQDs while maintaining Raman enhancement over the wide UV-Vis absorption of Mn_3O_4. The self-assembly process between the GQDs and Mn_3O_4 particles changes the energy level and gap. RhB, a Raman-active dye, was quenched efficiently on this nanocomposite substrate, the fluorescence background of the Raman signal was lower than that for the GQDs, and the Raman peaks matched previous reports. The EFs were as high as 2.06×10^4. The GQD–Mn_3O_4 nanocomposite possesses good biocompatibility and can be used as an active substrate for SERS identification of human cancer cells. Furthermore, the GQD–Mn_3O_4 nanocomposite improves the performance of graphene for Raman applications and paves the way for a new range of self-assembled nanocomposites, such as half-metallic graphene nanoribbons assembled with semiconductors or magnetic metal oxides with novel physical or chemical properties. We anticipate that GQD–Mn_3O_4 nanocomposites might open up new opportunities for the development of new bioanalytical and biomedical applications in SERS.

Acknowledgements

This work was supported by the National Natural Science Foundations of China (NSFC, Grant No. 21327007, 21305020, and 201575031), Natural Science Foundations of Guangxi Province (No. 2014GXNSFBA118041, and 2015GXNSFDA 139006), IRT1225, as well as BAGUI Scholar Program.

Notes and references

1 R. K. Khanna, *J. Chem. Phys.*, 1981, **74**, 2108–2115.
2 K. L. Wustholz, C. L. Brosseau, F. Casadio and R. P. Van Duyne, *Phys. Chem. Chem. Phys.*, 2009, **11**, 7350–7359.
3 S. Schlucker, *Angew. Chem.*, 2014, **53**, 4756–4795.
4 W. Xu, N. Mao and J. Zhang, *Small*, 2013, **9**, 1206–1224.
5 X. Xu, H. Li, D. Hasan, R. S. Ruoff, A. X. Wang and D. L. Fan, *Adv. Funct. Mater.*, 2013, **23**, 4332–4338.
6 A. Campion and P. Kambhampati, *Chem. Soc. Rev.*, 1998, **27**, 241–250.
7 X. M. Lin, Y. Cui, Y. H. Xu, B. Ren and Z. Q. Tian, *Anal. Bioanal. Chem.*, 2009, **394**, 1729–1745.
8 X. Liu, Y. Shao, Y. Tang and K. F. Yao, *Sci. Rep.*, 2014, **4**, 5835.
9 R. G. Freeman, K. C. Grabar, K. J. Allison, R. M. Bright, J. A. Davis, A. P. Guthrie, M. B. Hommer, M. A. Jackson, P. C. Smith, D. G. Walter and M. J. Natan, *Science*, 1995, **267**, 1629–1632.
10 B. Zhang, H. Wang, L. Lu, K. Ai, G. Zhang and X. Cheng, *Adv. Funct. Mater.*, 2008, **18**, 2348–2355.
11 M. Potara, D. Maniu and S. Astilean, *Nanotechnology*, 2009, **20**, 14059–14066.
12 X. Yu, H. Cai, W. Zhang, X. Li, N. Pan, Y. Luo, X. Wang and J. G. Hou, *ACS Nano*, 2011, **5**, 952–958.

13 S. Cong, Y. Yuan, Z. Chen, J. Hou, M. Yang, Y. Su, Y. Zhang, L. Li, Q. Li, F. Geng and Z. Zhao, *Nat. Commun.*, 2015, **6**, 7800.
14 X. Ling, L. Xie, Y. Fang, H. Xu, H. Zhang, J. Kong, M. S. Dresselhaus, J. Zhang and Z. Liu, *Nano Lett.*, 2010, **10**, 553–561.
15 X. Ling, L. G. Moura, M. A. Pimenta and J. Zhang, *J. Phys. Chem. C*, 2012, **116**, 25112–25118.
16 W. Xu, X. Ling, J. Xiao, M. S. Dresselhaus, J. Kong, H. Xu, Z. Liu and J. Zhang, *Proc. Natl. Acad. Sci. U. S. A.*, 2012, **109**, 9281–9286.
17 H. Cheng, Y. Zhao, Y. Fan, X. Xie, L. Qu and G. Shi, *ACS Nano*, 2012, **6**, 2237–2244.
18 J. Liu, H. Cai, X. Yu, K. Zhang, X. Li, J. Li, N. Pan, Q. Shi, Y. Luo and X. Wang, *J. Phys. Chem. C*, 2012, **116**, 15741–15746.
19 B. Trauzettel, D. V. Bulaev, D. Loss and G. Burkard, *Nat. Phys.*, 2007, **3**, 192–196.
20 K. A. Ritter and J. W. Lyding, *Nat. Mater.*, 2009, **8**, 235–242.
21 L. A. Ponomarenko, F. Schedin, M. I. Katsnelson, R. Yang, E. W. Hill, K. S. Novoselov and A. K. Geim, *Science*, 2008, **320**, 356–358.
22 S. Thongrattanasiri, A. Manjavacas and F. J. Garcia de Abajo, *ACS Nano*, 2012, **6**, 1766–1775.
23 D. Pan, J. Zhang, Z. Li and M. Wu, *Adv. Mater.*, 2010, **22**, 734–738.
24 S. Zhuo, M. Shao and S. T. Lee, *ACS Nano*, 2012, **6**, 1059–1064.
25 L. Xie, X. Ling, Y. Fang, J. Zhang and Z. Liu, *J. Am. Chem. Soc.*, 2009, **131**, 9890–9891.
26 J. R. Lombardi and R. L. Birke, *J. Phys. Chem. C*, 2008, **112**, 5605–5617.
27 L. F. d. Freitas and M. R. Hamblin, in *Antimicrobial Photodynamic Inactivation and Antitumor Photodynamic Therapy with Fullerenes*, Morgan & Claypool Publishers, 2016, p. 4, DOI: 10.1088/978-1-6817-4247-2ch4.
28 J. L. Chen, X. P. Yan, K. Meng and S. F. Wang, *Anal. Chem.*, 2011, **83**, 8787–8793.
29 A. Marchioro, J. Teuscher, D. Friedrich, M. Kunst, R. van de Krol, T. Moehl, M. Grätzel and J.-E. Moser, *Nat. Photonics*, 2014, **8**, 250–255.
30 A. V. Akimov, A. J. Neukirch and O. V. Prezhdo, *Chem. Rev.*, 2013, **113**, 4496–4565.
31 Q. Li, L. Hong, H. Li and C. Liu, *Biosens. Bioelectron.*, 2017, **89**, 477–482.
32 X. Wang, W. Shi, G. She and L. Mu, *J. Am. Chem. Soc.*, 2011, **133**, 16518–16523.
33 J. R. Lombardi and R. L. Birke, *J. Phys. Chem. C*, 2014, **118**, 11120–11130.
34 Y. Li, Y. Hu, Y. Zhao, G. Shi, L. Deng, Y. Hou and L. Qu, *Adv. Mater.*, 2011, **23**, 776–780.
35 L. Tang, R. Ji, X. Li, K. S. Teng and S. P. Lau, *J. Mater. Chem. C*, 2013, **1**, 4908–4915.
36 Z. L. Wu, M. X. Gao, T. T. Wang, X. Y. Wan, L. L. Zheng and C. Z. Huang, *Nanoscale*, 2014, **6**, 3868–3874.
37 G. M. Whitesides and B. Grzybowski, *Science*, 2002, **295**, 2418–2421.
38 G. P. Acuna, F. M. Moller, P. Holzmeister, S. Beater, B. Lalkens and P. Tinnefeld, *Science*, 2012, **338**, 506–510.
39 S. M. Douglas, I. Bachelet and G. M. Church, *Science*, 2012, **335**, 831–834.
40 I. L. Medintz, A. R. Clapp, H. Mattoussi, E. R. Goldman, B. Fisher and J. M. Mauro, *Nat. Mater.*, 2003, **2**, 630–638.
41 Y. Xu, Q. Wu, Y. Sun, H. Bai and G. Shi, *ACS Nano*, 2010, **4**, 7358–7362.
42 N. Li, G. Liu, C. Zhen, F. Li, L. Zhang and H.-M. Cheng, *Adv. Funct. Mater.*, 2011, **21**, 1717–1722.
43 D. Wang, R. Kou, D. Choi, Z. Yang, Z. Nie, J. Li, L. V. Saraf, D. Hu, J. Zhang, G. L. Graff, J. Liu, M. A. Pope and I. A. Aksay, *ACS Nano*, 2010, **4**, 1587–1595.
44 D. Wang, D. Choi, J. Li, Z. Yang, Z. Nie, R. Kou, D. Hu, C. Wang, L. V. Saraf, J. Zhang, I. A. Aksay and J. Liu, *ACS Nano*, 2009, **3**, 907–914.
45 Z. Tang, S. Shen, J. Zhuang and X. Wang, *Angew. Chem.*, 2010, **49**, 4603–4607.
46 H. P. Cong, X. C. Ren, P. Wang and S. H. Yu, *ACS Nano*, 2012, **6**, 2693–2703.
47 J. W. Lee, A. S. Hall, J.-D. Kim and T. E. Mallouk, *Chem. Mater.*, 2012, **24**, 1158–1164.
48 L. Li, Z. Guo, A. Du and H. Liu, *J. Mater. Chem.*, 2012, **22**, 3600–3605.
49 J. R. Lombardi, R. L. Birke, T. Lu and J. Xu, *J. Chem. Phys.*, 1986, **84**, 4174–4180.
50 X. Hao, J. Zhao, Y. Li, Y. Zhao, D. Ma and L. Li, *Colloids Surf., A*, 2011, **374**, 42–47.
51 Z. Zhao, H. Fan, G. Zhou, H. Bai, H. Liang, R. Wang, X. Zhang and W. Tan, *J. Am. Chem. Soc.*, 2014, **136**, 11220–11223.
52 R. Deng, X. Xie, M. Vendrell, Y. T. Chang and X. Liu, *J. Am. Chem. Soc.*, 2011, **133**, 20168–20171.
53 D. V. Kosynkin, A. L. Higginbotham, A. Sinitskii, J. R. Lomeda, A. Dimiev, B. K. Price and J. M. Tour, *Nature*, 2009, **458**, 872–876.
54 T. S. Sreeprasad, A. A. Rodriguez, J. Colston, A. Graham, E. Shishkin, V. Pallem and V. Berry, *Nano Lett.*, 2013, **13**, 1757–1763.
55 P. Russo, A. Hu, G. Compagnini, W. W. Duley and N. Y. Zhou, *Nanoscale*, 2014, **6**, 2381–2389.
56 T. Palaniselvam, M. O. Valappil, R. Illathvalappil and S. Kurungot, *Energy Environ. Sci.*, 2014, **7**, 1059.
57 W. Qian, Z. Chen, S. Cottingham, W. A. Merrill, N. A. Swartz, A. M. Goforth, T. L. Clare and J. Jiao, *Green Chem.*, 2012, **14**, 371–377.
58 L. Zhang, Q. Zhou, Z. Liu, X. Hou, Y. Li and Y. Lv, *Chem. Mater.*, 2009, **21**, 5066–5071.
59 S. Park, K. S. Lee, G. Bozoklu, W. Cai, S. T. Nguyen and R. S. Ruoff, *ACS Nano*, 2008, **2**, 572–578.
60 J. Duan, S. Chen, S. Dai and S. Z. Qiao, *Adv. Funct. Mater.*, 2014, **24**, 2072–2078.
61 M. Baldi, F. Milella, J. M. Gallardo-Amores and G. Busca, *J. Mater. Chem.*, 1998, **8**, 2525–2531.
62 A. Vazquez-Olmos, R. Redon, G. Rodriguez-Gattorno, M. Esther Mata-Zamora, F. Morales-Leal, A. L. Fernandez-Osorio and J. M. Saniger, *J. Colloid Interface Sci.*, 2005, **291**, 175–180.

63 D. M. Adams and P. J. Lock, *J. Chem. Soc. A*, 1971, 2801, DOI: 10.1039/j19710002801.
64 J. Zhang, X. Li, X. Sun and Y. Li, *J. Phys. Chem. B*, 2005, **109**, 12544–12548.
65 S. Shim, C. M. Stuart and R. A. Mathies, *ChemPhysChem*, 2008, **9**, 697–699.
66 J. Sarkar, J. Chowdhury, P. Pal and G. B. Talapatra, *Vib. Spectrosc.*, 2006, **41**, 90–96.
67 L. D. Gelb and K. E. Gubbins, *Langmuir*, 1998, **14**, 2097–2111.
68 X. Ling, J. Wu, W. Xu and J. Zhang, *Small*, 2012, **8**, 1365–1372.
69 X. Ling and J. Zhang, *Small*, 2010, **6**, 2020–2025.
70 K. Hashimoto, M. Hiramoto and T. Sakata, *Chem. Phys. Lett.*, 1988, **148**, 215–220.
71 Y. Li, Y. Zhao, H. Cheng, Y. Hu, G. Shi, L. Dai and L. Qu, *J. Am. Chem. Soc.*, 2012, **134**, 15–18.
72 B. Yan, A. Thubagere, W. R. Premasiri, L. D. Ziegler, L. Dal Negro and B. M. Reinhard, *ACS Nano*, 2009, **3**, 1190–1202.
73 K. M. Omberg, J. C. Osborn, S. L. Zhang, J. P. Freyer, J. R. Mourant and J. R. Schoonover, *Appl. Spectrosc.*, 2002, **56**, 813–819.